ACS Catalysis

Research Article

pubs.acs.org/acscatalysis

Domain-Confined Multiple Collision Enhanced Catalytic Soot Combustion over a Fe_2O_3/TiO_2–Nanotube Array Catalyst Prepared by Light-Assisted Cyclic Magnetic Adsorption

Yifu Yu, Jiale Ren, Dongsheng Liu, and Ming Meng*

Collaborative Innovation Center for Chemical Science and Engineering (Tianjin), Tianjin Key Laboratory of Applied Catalysis Science & Engineering, School of Chemical Engineering & Technology, Tianjin University, Tianjin 300072, P. R. China

Supporting Information

ABSTRACT: The ordered TiO_2 nanotube array (NA)-supported ferric oxide nanoparticles with adjustable content and controllable particulate size were prepared through a facile light-assisted cyclic magnetic adsorption (LCMA) method. Multiple techniques such as SEM, TEM, EDX, XRD, EXAFS, XPS, UV–vis absorption, and TG were employed to study the structure and properties of the catalysts. The influencing factors upon soot combustion including the annealing temperature and loading of the active component in Fe_2O_3/TiO_2–NA were also investigated. An obvious confinement effect on the catalytic combustion of soot was observed for the ferric oxide nanoparticles anchored inside TiO_2 nanotubes. On the basis of the catalytic performance and characterization results, a novel domain-confined multiple collision enhanced soot combustion mechanism was proposed to account for the observed confinement effect. The design strategy for such nanotube array catalysts with domain-confined macroporous structure is meaningful and could be well-referenced for the development of other advanced soot combustion catalysts.

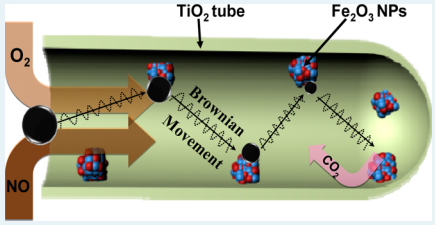

KEYWORDS: *Fe_2O_3/TiO_2–nanotubes, magnetic adsorption, confinement effect, soot combustion, multiple collision*

INTRODUCTION

The emission control of gasoline and diesel soot has attracted more and more attention, because it can give rise to serious environmental and health problems.[1−3] The combination of oxidation catalysts and particulate filters in the continuously regenerated particulate trap is now regarded as the most promising after-treatment technique for the removal of soot particulates in gasoline and diesel exhaust.[4] Catalysts coated on filters are required to possess high soot combustion activity in the low temperature region and good thermal stability under practical working conditions.[5] At present, the research studies are mainly focused on developing catalysts with lower soot ignition temperature.[6−17] It is well-known that the reaction of catalytic soot combustion is a typical redox process in nature, which takes place at the "triple-phase contact points" among solid catalyst, soot particulate, and gaseous reactant. The oxidation ability, the number of contact points as well as the contact efficiency are particularly important for catalytic soot combustion. Thus, the design and choice of soot combustion catalysts usually proceed in three ways. The first way is to improve the oxidation ability of the catalysts by using various kinds of methods, such as adding additives,[6] enhancing interaction between supports and active component,[7] ion doping,[8] and adopting composite oxide.[9,10] The second way is to increase the tangible active points between reactants and catalysts by increasing the catalyst surface area or enhancing the dispersion of active phases.[11,12] The third way is to improve the contact efficiency by adding the components with high mobility or relatively low melting points (potassium- or chloride-containing compounds) into catalysts to wet the soot particulates.[13−17] However, in the second way, the effect of increasing catalyst surface area or decreasing catalyst particle size is very limited, because the soot particulates can hardly penetrate into the micropores or mesopores of the catalysts. In the third way, the components with high mobility and relatively low melting points such as basic metal oxides often possess good solubility in water, which can induce remarkable loss of these components in water-containing emission, decreasing the performance and durability of the catalysts.[18,19] Recently, Zhao and co-workers designed a series of three-dimensionally ordered macroporous oxides to improve the contact efficiency between soot particulates and catalysts, which exhibited higher catalytic activity for soot oxidation as compared with the disordered macroporous and nanoparticle-based samples.[20,21] The employment of ordered macroporous materials can greatly increase the contact points, because the inner surface of macropores is also accessible to soot particulates. So, it is believed that the catalytic activity of the catalysts for soot combustion can be remarkably improved through reasonable design on the morphology of catalysts.

Herein, we employed a facile method, namely, light-assisted cyclic magnetic adsorption (LCMA), to synthesize the ordered

Received: November 3, 2013
Revised: January 27, 2014
Published: February 4, 2014

TiO_2 nanotube-array-supported ferric oxide nanoparticles[22] with adjustable content and controllable particle size. The as-prepared catalysts possess uniform macroporous structure (~140 nm) and high catalytic activity for soot combustion. Such domain-confined macroporous structure is large enough to allow entrance of soot particulates; the entered soot particulates will produce Brownian-like movement in the reaction gas flow with high space velocity, and as a result, these particulates may contact the active sites on the inner surface of nanotubes through multiple collisions. This is favorable to the total combustion of soot particulates, because their large size (~30 nm) makes the oxidation process scarcely finished at the moment of a single collision. Compared with the open structure of particle-based catalysts with only outer surface accessible, the half-closed tube structure of the ordered TiO_2 nanotubes is obviously more favorable to the soot combustion, which is different from the situation for the molecular collision reaction. On the basis of SEM, TEM, EDX, XRD, EXAFS, XPS, UV−vis absorption, and TG characterization results, the correlation between the structures and catalytic performance was elucidated, and a novel multiple collision mechanism for soot combustion was proposed.

EXPERIMENTAL SECTION

Sample Preparation. The TiO_2 nanotube array (TiO_2−NA) was fabricated by anodization as described previously.[23] The TiO_2−NA-supported Fe_2O_3 nanoparticles (Fe_2O_3/TiO_2−NA) were prepared via the light-assisted cyclic magnetic adsorption (LCMA) method developed in our lab. The diagram of the preparation process is displayed in Figure 1. In one typical LCMA cycle, the sample of Fe_3O_4 nanoparticles was first prepared through coprecipitation according to ref 24. Given amounts of $FeSO_4{\cdot}7H_2O$ and $Fe_2(SO_4)_3$ were first dissolved in water, and ammonia−water (25%) was subsequently added dropwise to adjust the pH to 10. Then, the reaction mixture was stirred for 1 h at 60 °C to produce the Fe_3O_4 nanoparticles. The surface of Fe_3O_4 nanoparticles was modified by oleic acid (OC) through strong stirring adsorption. Then, the obtained Fe_3O_4−OC suspension (5 mL 0.1M) was transferred into a self-made quartz square cylinder. In the next step, the as-prepared TiO_2−NA support was pretreated under a 300 W Xe light source for a 0.5 h irradiation to make its surface totally hydrophilic. Afterward, this hydrophilic TiO_2−NA was deposited at the bottom of the square cylinder filled with a Fe_3O_4−OC suspension, and a circular magnet (30 × 10 mm, 13.0 KGS) was put under the cylinder to drive the nanoparticles of Fe_3O_4−OC into TiO_2 nanotubes (a photograph of the experimental apparatus was displayed in Figure S1). After 5 min, the titanium sheet was picked up with tweezers and rinsed with water for 10 s to remove the excess precursor solution, and at this point, one cycle was finished. This cycle was repeated for 2, 5, and 10 times. After annealing at 500 °C for 4 h, the supported Fe_3O_4−OC nanoparticles were transformed into Fe_2O_3 nanoparticles, and the desired catalysts Fe_2O_3/TiO_2−NA were obtained and denoted as 2FeTi, 5FeTi, and 10FeTi, respectively. Through catalytic activity screening, the series of five-cycle samples were chosen for further research. To investigate the effect of calcination temperature on activity, the five-cycle samples are calcined in static air for 4 h at several temperatures including 500, 600, and 700 °C. The obtained catalysts are denoted as FeTi-T, where T represents the calcination temperature. The Fe_2O_3 content of the obtained FeTi-T catalyst was 8 wt %.

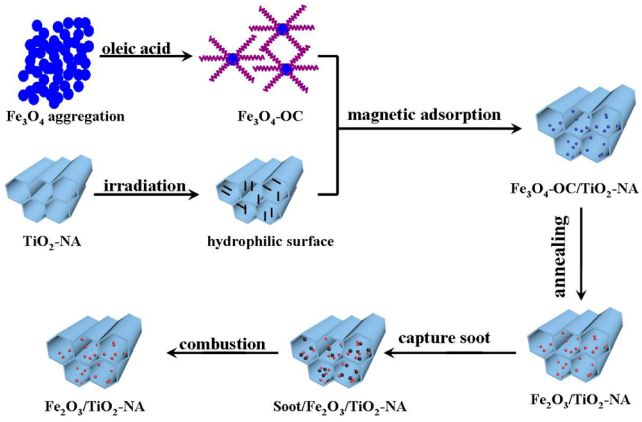

Figure 1. Schematic diagram of the light-assisted cyclic magnetic adsorption (LCMA) method used for the synthesis of the catalysts Fe_2O_3/TiO_2−NA with the catalytic soot oxidation process.

The sample Fe_2O_3/TiO_2−P (also 8 wt % Fe_2O_3) was used as a reference catalyst for comparison. The TiO_2 powder (TiO_2−P) with a BET surface area of 43 m^2/g was obtained by a thermal treatment of the commercial TiO_2 powder (P25, Degussa, BET surface area 50 m^2/g) at 500 °C for 10 h. The Fe_2O_3/TiO_2−P catalyst was prepared by impregnation of the TiO_2−P into aqueous $Fe(NO_3)_3{\cdot}9H_2O$ solution and calcined at 500 °C for 4 h in air.

Characterization. The morphology of the samples was studied by a transmission electron microscope (JEOL-2100F) and field-emission scanning electron microscope (S-4800, Hitachi) equipped with an energy-dispersive X-ray analyzer (Thermo Scientific).

The X-ray diffraction patterns (XRD) of the products were recorded with a Bruker D8 diffraction meter using Cu Kα (λ = 0.15418 nm) as radiation source. UV−vis diffuse reflectance spectra were recorded by a Lambda 750S UV−vis spectrometer (Perkin-Elmer) with an integrating sphere. The specific surface area (SSA) was measured at −196 °C on a Quantachrome QuadraSorb SI instrument using the nitrogen adsorption method. The samples were pretreated in a vacuum at 200 °C for 10 h before experiments. The surface area was determined by BET method in 0−0.3 partial pressure range.

The spectra of extended X-ray absorption fine structure (EXAFS) were obtained using the instruments at Beijing Synchrotron Radiation Facility (BSRF) at ~150 mA and ~2.2 GeV. The X-ray absorption spectra of the Fe *K*-edge of the samples were recorded in fluorescence mode, and those for reference compounds were recorded in transmission mode.

The X-ray photoelectron spectra (XPS) were carried out with PHI-1600 ESCA spectrometer using Mg Kα radiation (1253.6 eV) as X-ray source. The binding energy was calibrated using C1s peak (BE = 284.6 eV) as standard and quoted with a precision of ±0.2 eV. The atomic composition of the samples at the surface was calculated.

Activity Evaluation. The catalytic activity of the prepared catalysts for soot combustion was evaluated by the TG/DTA technique using commercial soot (Printex-U, Degussa) as reactant. First, the soot was dispersed in ethanol under ultrasonic assistance. In the next step, the produced suspension was dropped on the surface of the catalysts and dried at 60 °C. In the whole process, the deposition of soot on the catalyst surface is driven by gravity; no grinding or mechanical mixing was performed. The weight ratio of soot to catalyst is 1:20. The mixture of soot and catalyst was then heated from room temperature to 700 °C at a slope of 5 °C min^{-1} in an atmosphere of 600 ppm NO, 10 vol % O_2 and balanced N_2 with a flow rate of 50 mL min^{-1}. T_{ig} is defined as the temperature at which 5% of the soot was oxidized. After the temperature-programmed oxidation experiment, a DTG curve with a complete weight loss peak was obtained; the *y*-axis value of the peak zenith corresponds to the largest weight loss rate (R_{max}). In this work, the ignition temperature for soot combustion (denoted as T_{ig}) over different catalysts was compared to evaluate their catalytic performance.

The apparent activation energy (E_a) for soot combustion over the catalysts was measured by TG/DTA techniques, according to the reported Ozawa method.[25,26] The activation energy was calculated by the following equation:

$$\ln B = -0.4657\frac{E_a}{R}\frac{1}{T} + C$$

dx.doi.org/10.1021/cs401017r | ACS Catal. 2014, 4, 934−941

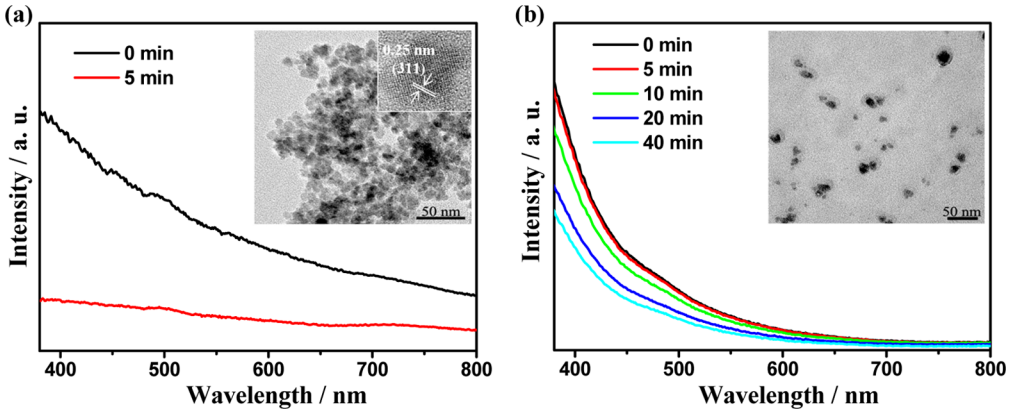

Figure 2. UV−vis absorption spectra for the samples Fe_3O_4 (a) and Fe_3O_4−OC (b) after centrifugation (2000 r/min) for different times. Inset in (a): TEM images of Fe_3O_4. Inset in (b): TEM images of Fe_3O_4−OC.

In the equation, C is a constant, and B is the heating rate. In this work, three different heating rates (B_1 = 2 °C/min, B_2 = 5 °C/min, B_3 = 10 °C/min) were used for catalytic soot combustion. Each pair of ln B and $1/T$ of these data were used for plotting based on a 20% conversion of soot. From the above equation, E_a could be calculated from the slope of the plotted line.

RESULTS AND DISCUSSION

Figure 2 shows the effect of oleic acid adsorption on the dispersion degree of as-prepared Fe_3O_4 nanoparticles. The TEM image (inset of Figure 2a) shows that the Fe_3O_4 nanoparticles prepared through coprecipitation tended to accumulate together. After modification of oleic acid, the dispersion of the nanoparticles Fe_3O_4−OC was improved obviously, and a layer of organic compounds could be clearly observed on the surface of Fe_3O_4 nanoparticles (inset in Figure 2b), which indicates that the surface adsorption of oleic acid on Fe_3O_4 nanoparticles was achieved through simple stirring. It has been reported that the surface-adsorbed organics could strengthen the electrostatic repulsive force and the space resistance among nanoparticles, making them better dispersed.[27,28] The results of UV−vis spectra also support this conclusion. After 5 min of centrifugation, almost all the Fe_3O_4 nanoparticles subsided to the bottom owing to the large size of aggregation, resulting in the disappearance of UV−vis absorption peaks, as shown in Figure 2a. At the same time, the UV−vis absorption intensity of the Fe_3O_4−OC solution changed minimally even after 40 min of centrifugation, as seen in Figure 2b. These results clarify that highly dispersed Fe_3O_4 nanoparticles have been successfully synthesized through coprecipitation and subsequent oleic acid modification.

The next step is to drive the Fe_3O_4−OC nanoparticles into TiO_2 nanotubes as displayed in Figure 1. To simultaneously achieve high dispersion and free deposition for Fe_3O_4−OC nanoparticles, a magnetic field was introduced into the system in light of the superparamagnetism of Fe_3O_4 nanoparticles.[24] Without external magnetic force, the Fe_3O_4−OC suspension remained unchanged even after 30 min of stewing, as observed in Figure 3a (middle bottle); however, in the presence of a magnetic field, the Fe_3O_4−OC nanoparticles totally subsided to the bottom of the square cylinder within 3 min. However, at distinct areas, the loading amounts of Fe_3O_4 nanoparticles on the TiO_2 substrate are different (Figure S2) if we directly put the tubes array into the cylinder. It was found that the Fe content at certain points decreases with increasing distance from the center, and there is almost no peak for Fe species at

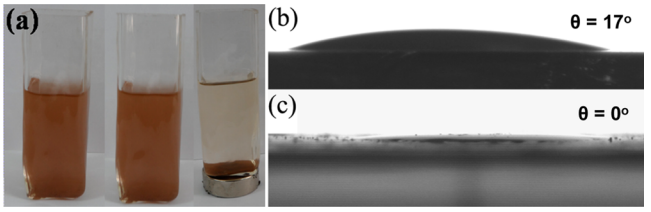

Figure 3. (a) Photographs of Fe_3O_4−OC suspension in the square cylinder. From left to right: the precursor suspension, the suspension after stewing for 30 min, and the suspension after magnetic adsorption for 3 min. (b) Contact angle of water on TiO_2 nanotubes. (c) Contact angle of water on the same TiO_2 nanotubes after exposure to irradiation for 30 min.

the edge of the substrate (region III). It is known that after exposure to irradiation, the surface of TiO_2 could turn hydrophilic, which has been widely applied in self-cleaning materials research.[29,30] Thus, the light irradiation pretreatment on TiO_2−NA was performed before magnetic-assisted adsorption. The effect of irradiation on contact angle could be seen in Figure 3b,c. It is clear that the contact angle changed from 17° to 0° after exposure to irradiation for 30 min, suggesting its good hydrophilicity. In addition, the distribution of Fe_3O_4 nanoparticles on the TiO_2 nanotube array became uniform when the employed TiO_2−NA was pretreated by irradiation, as confirmed by the similar Fe/Ti ratio at different regions (Figure 4 and Table 1). The nearly unchanged Fe/Ti ratio demonstrates that the irradiation facilitated the dispersion of Fe_3O_4 nanoparticles. This may be due the hydrophilic surface allowing the suspension to enter the nanotubes more easily, weakening the function of the uneven distribution of the magnetic field.

To select an appropriate temperature for annealing of the catalysts, the TG analysis on Fe_3O_4 and Fe_3O_4−OC nanoparticles (Figure 5) was carried out. It is shown that the surface-adsorbed oleic acid could be completely removed at 400 °C. Considering the practical operation condition for soot oxidation catalysts, higher annealing temperatures such as 500, 600, and 700 °C were adopted for investigating the annealing temperature effect on catalytic activity. In addition, from the TG results, the adsorbed oleic acid content in the obtained Fe_3O_4−OC nanoparticles was calculated (~11 wt %).

In order to prove the existence of Fe_2O_3 in the catalysts FeTi-T and Fe_2O_3/TiO_2−P, the Fe K-edge EXAFS characterization was performed on these catalysts and the reference

dx.doi.org/10.1021/cs401017r | ACS Catal. 2014, 4, 934−941

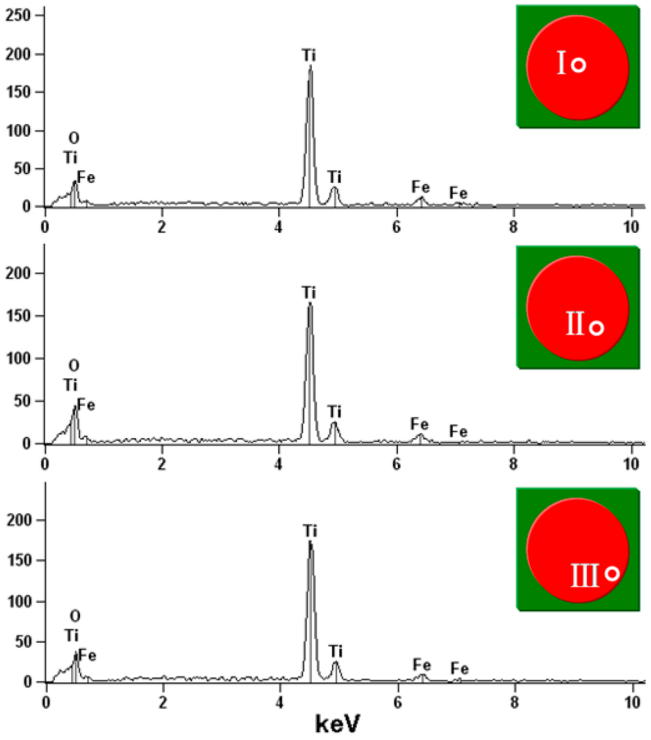

Figure 4. EDS spectra for Fe_3O_4−OC/TiO_2−NA samples prepared through the LCMA method after five times of cyclic adsorption. The schematic diagrams illustrate where the electron beam was aligned when the corresponding EDS spectrum was acquired.

Table 1. Molar Ratios of Fe to Ti in the Sample Fe_3O_4−OC/TiO_2−NA with and without Light Assistance, Measured at Different Regions As Shown in Figure 4 and Figure S2

sample	I	II	III
Fe_3O_4−OC/TiO_2−NA[a]	0.24	0.13	0.02
Fe_3O_4−OC/TiO_2−NA[b]	0.09	0.08	0.08

[a]Without light assistance. [b]With light assistance.

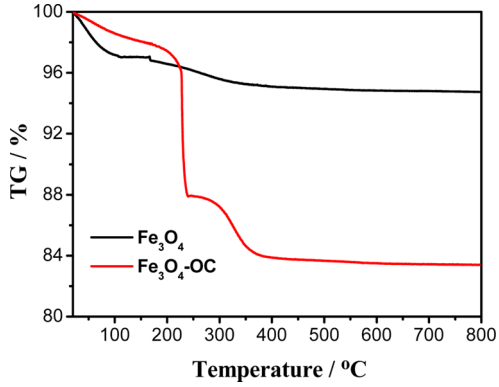

Figure 5. TG curves of Fe_3O_4 nanoparticles with or without oleic acid modification.

Fe_2O_3, the results of which are shown in Figure 6. The similarity of the Fe *K*-edge radial structure functions (RSFs) of these catalysts to that of the reference Fe_2O_3 verifies that the Fe_2O_3 species do exist in all the FeTi-T and Fe_2O_3/TiO_2−P catalysts. All the RSFs show two major coordination peaks. The first one appearing at 0.14 nm (not corrected by phase scattering shift) is assigned to the Fe−O shell (one Fe

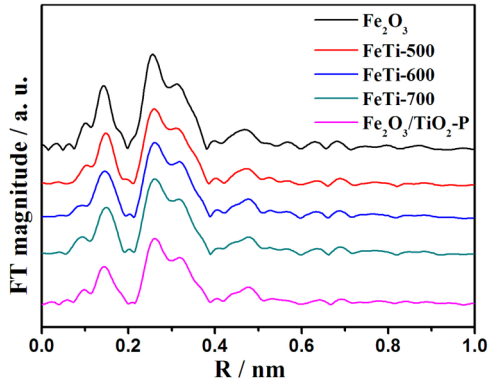

Figure 6. Fe *K*-edge radial structure functions of the as-prepared catalysts and reference compound Fe_2O_3.

coordinating with 3 O atoms), and the second one with the maximum around 0.26 nm is contributed by the Fe−Fe shell (one Fe coordinating with 4 Fe atoms).[31,32] The presence of Fe_2O_3 species identified by EXAFS and the absence of corresponding diffraction signals in the XRD patterns (Figure S3) suggest that the Fe_2O_3 nanoparticles have been successfully anchored in TiO_2 nanotubes, which possess high dispersion.

Figure 7 shows the results of UV−vis diffuse reflectance spectra of TiO_2−NA, Fe_2O_3−P, and FeTi-T catalysts. The

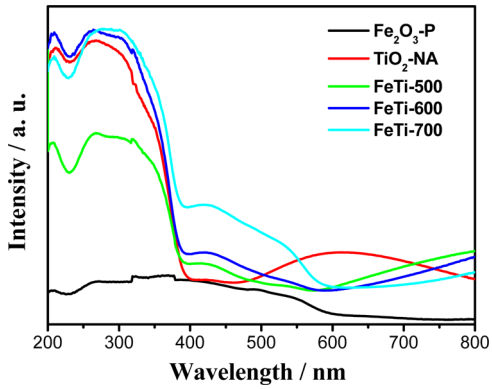

Figure 7. UV−vis diffuse reflectance absorption spectra of the as-prepared catalysts.

characteristic absorption of anatase TiO_2 induced by d−d electron transition can be clearly observed for TiO_2−NA, whose edge is at ∼390 nm by extrapolating the steep slopes of the curve. The sample Fe_2O_3−P exhibits very wide absorption from 200 to 600 nm. As to the catalysts FeTi-T, except for the characteristic absorption of anatase TiO_2, new absorption in the range of 400−600 nm is observed, whose intensity increases with the elevation of annealing temperature, indicating the coexistence of TiO_2−NA and Fe_2O_3 nanoparticles in the FeTi-T catalysts.[23,33−35]

The morphology and microstructure of TiO_2−NA and the catalyst FeTi-500 were characterized by SEM and TEM, as displayed in Figure 8. The top-view SEM image of TiO_2−NA (Figure 8a) shows that the TiO_2−NA has ordered macropores with a diameter of ∼150 nm, and the side-view SEM images of TiO_2−NA (Figure 8b and its inset) indicate that the length of the TiO_2 nanotubes can reach ∼20 μm. The TEM image (Figure 8c) demonstrates that the inner of TiO_2−NA is clean and empty. After they were used in magnetic enhanced adsorption of Fe_3O_4−OC nanoparticles and subsequent

dx.doi.org/10.1021/cs401017r | ACS Catal. 2014, 4, 934−941

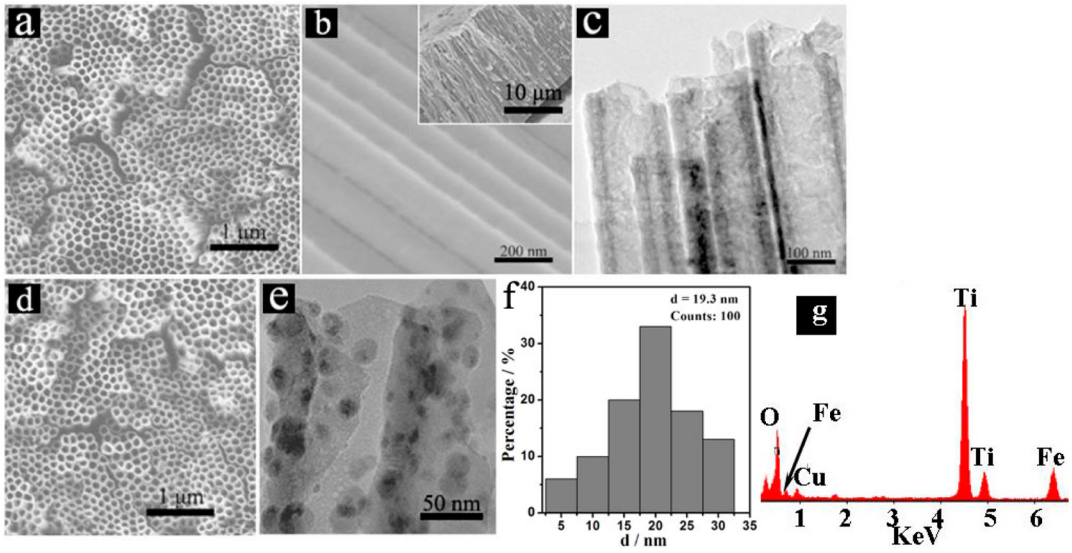

Figure 8. Electron microscope characterization on the samples TiO_2−NA (a−c) and FeTi-500 (d−g): (a) SEM image (top view); (b) SEM image (side view); (c) TEM image; (d) SEM image (top view) of the FeTi-500; (e) TEM image; (f) size distribution of Fe_2O_3 nanoparticles; (g) the EDS spectrum of the sample.

Table 2. O1s Binding Energy (BE), the Percentages of Different Surface Oxygen Species, the Average Particle Sizes, the Ignition Temperature (T_{ig}), and the Apparent Activation Energy (E_a) for Soot Combustion

catalysts	BE of O1s (eV)	percentages	particle size (nm)	T_{ig} (°C)	E_a (kJ/mol)
Fe_2O_3/TiO_2−P	529.5[a]/531.4[b]	0.42[a] /0.58[b]	12.3	358	110
FeTi-500	529.9[a]/531.4[b]	0.70[a] /0.30[b]	19.3	315	70
FeTi-600	529.7[a]/531.6[b]	0.83[a] /0.17[b]	20.2	345	71
FeTi-700	529.7[a]/531.7[b]	0.91[a] /0.09[b]	21.5	387	79

[a]Surface lattice oxygen. [b]Surface-adsorbed oxygen.

thermal annealing at 500 °C, the arranged hexagonal nanotubes with vertical orientation are well-represented, as shown in Figure 8d. The presence of Fe_2O_3 nanoparticles in the inner TiO_2 nanotubes can be clearly observed from the TEM in Figure 8e. These nanoparticles possess an average diameter of 19.3 nm (Figure 8f). With an increase in annealing temperature, the size of Fe_2O_3 nanoparticles in FeTi-T catalysts did not change much (Table 2), still close to that of the FeTi-500 and Fe_3O_4−OC precursor nanoparticles. This result suggests that the size of the supported nanoparticles can be effectively controlled through the separation of nanoparticle synthesis and the loading process during preparation. Moreover, the loading amounts of active component can be easily adjusted through changing the cycle times (Figure S4 and Table S1). The EDX analysis shows that the nanoparticles in FeTi-500 are mainly composed of Fe and O elements (Figure 8g). All the above results demonstrate that the newly developed LCMA method is feasible to synthesize nanotube-supported nanoparticles with tunable size and adjustable loading amounts.

The activity of catalysts for soot combustion is displayed in Table S1, Figure 9, and Table 2. For comparison, the powder Fe_2O_3/TiO_2−P, TiO_2−P, and TiO_2−NA were also employed for catalytic soot combustion. First, the catalytic activities of the samples with different Fe loading show the following order: 5FeTi > 2FeTi > 10FeTi, indicating the existence of an optimal loading for Fe_2O_3 in TiO_2−NA (Table S1). For 2FeTi, the active sites may be too few (Figure S4a), so that the soot particulates cannot be eliminated efficiently. The sample 10FeTi with the highest amount of active component exhibits the worst catalytic activity for soot elimination, which can be

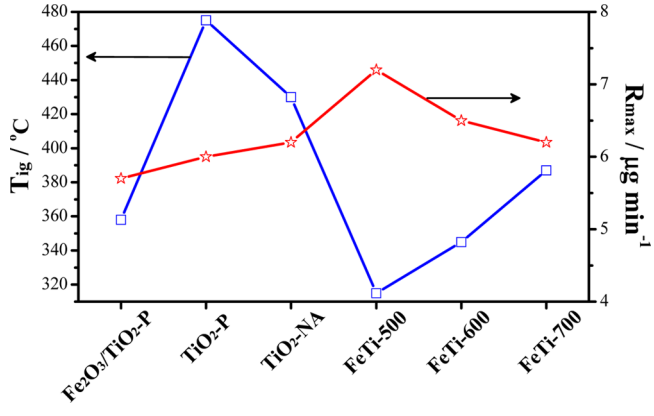

Figure 9. Catalytic soot combustion activity of different catalysts. Left: T_{ig} (the ignition temperature). Right: R_{max} (the maximal soot combustion rate).

attributed to the fact that too many Fe_2O_3 nanoparticles exist in the inner TiO_2 tubes (Figure S4b), blocking the enterance of soot particulates into the tubes. On the basis of this result, the series of 5FeTi catalysts with ∼8 wt % Fe_2O_3 were investigated in detail in this work. Compared with TiO_2−P, TiO_2−NA, and Fe_2O_3/TiO_2−P, the sample FeTi-500 exhibits higher catalytic activity for soot combustion. With the increase of calcination temperature, the catalytic activity of the samples FeTi-T markedly decreases. The results of XPS (Figure 10 and Table 2) show that the content of surface-adsorbed oxygen decreases in the following order: FeTi-500 > FeTi-600 > FeTi-700, which

dx.doi.org/10.1021/cs401017r | ACS Catal. 2014, 4, 934−941

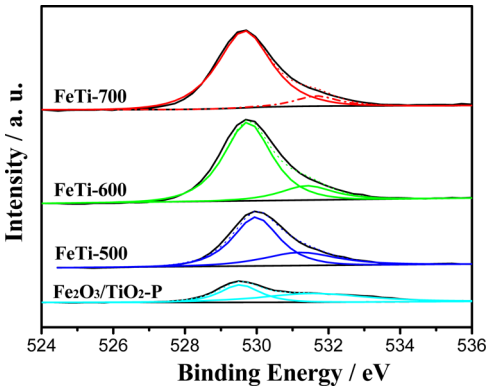

Figure 10. XPS spectra of O1s binding energy for different catalysts.

is in good accordance with the activity order for these catalysts. So, it is deduced that the surface-adsorbed oxygen is an important factor influencing the performance of FeTi-based catalysts for soot combustion. It should be noted that for the powder sample Fe_2O_3/TiO_2−P, although it has more surface-adsorbed oxygen, it displays worse catalytic activity than FeTi-500, which implies different mechanisms for powder and nanotube-based catalysts, as discussed later. The activity difference between FeTi-500 and Fe_2O_3/TiO_2−P can be elucidated from several aspects: (1) Although the powder TiO_2−P supported catalyst Fe_2O_3/TiO_2−P possesses considerable specific surface area (32 m^2/g) and small pore size around 2.1 nm (Figure S5), only the outer surface of the catalyst could be available to soot particulates due to their much larger size, because in this work loose contact mode between soot and catalyst (stirring with a spatula for 5 min) was employed. (2) The tube structure of TiO_2−NA possesses a high aspect ratio (~130/1) and large macroporous structure (~150 nm), both of which are favorable to the contact between soot and catalyst. (3) There may exist a positive confinement effect on soot combustion when soot particulates are restricted inside the nanotubes, and similar confinement effect was revealed on carbon nanotubes.[36] As to the essence of the confinement effect of the TiO_2−NA-based catalyst for soot combustion, it will be discussed in detail in the next section.

The underlying mechanism for soot oxidation is difficult to study because of the complexity of the catalytic system. In direct contact modes, Baker and Harris clearly observed the catalysts physically contacting with the edges or steps of soot by in situ transmission electron microscopy.[37,38] The surface lattice oxygen of the catalysts was identified as the active oxygen species, which can oxidize soot to carbon dioxide, thereby forming a surface oxygen vacancy. The as-formed surface oxygen vacancy was then filled up by the dissociative adsorbed oxygen, as shown in Scheme 1a. However, in reality, a great deal of soot can barely make direct contact with the catalysts. So, the catalytic soot combustion in the case of indirect contact should be taken into account. It is known that the migration or spillover of active species such as oxygen or hydrogen spillover can account well for the remote controlled catalytic oxidation or reduction. In NO_x-aided soot combustion, both the gas-phase transfer mechanism[39] and the surface spillover mechanism[40,41] were proposed. For the gas-phase transfer mechanism, the NO was first adsorbed and then oxidized by the active oxygen species on the catalyst surface, forming gaseous NO_2, which desorbed and transferred to the remote soot sites through the gas phase, thus enhancing soot

Scheme 1. Illustration of Different Catalytic Mechanisms for Soot Combustion: (a) Direct Contact Mechanism; (b) Indirect Contact Mechanism; (c) Domain-Confined Multiple Collision Mechanism for Soot Combustion on Fe_2O_3/TiO_2−NA Catalysts

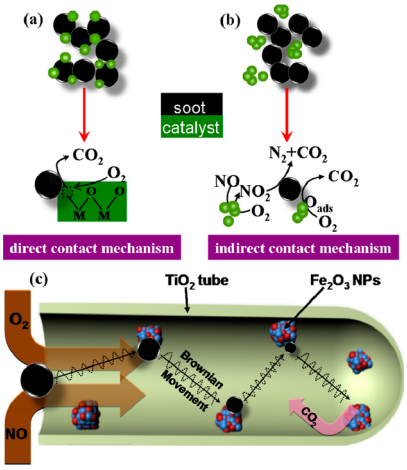

combustion. For the surface spillover mechanism, the adsorbed and activated oxygen species on the catalyst surface spilled over to the remote soot sites to oxidize the soot species. The gas-phase mechanism and the spillover mechanism are summarized in Scheme 1b. Of course, the direct/indirect contact soot oxidation can simultaneously occur during soot combustion, which has been confirmed by the oxygen-labeled investigation.[42]

In this work, an obvious confinement effect on the catalytic soot combustion can be observed for macroporous nanotube-based catalysts FeTi-T. Why did the Fe_2O_3 nanoparticles anchored into the TiO_2 nanotubes exhibit higher catalytic activity for soot oxidation than those supported on powder TiO_2−P? According to the EXAFS results of Fe *K*-edge (Figure 6) of the catalysts, it is thought that the bulk species of Fe in both FeTi-T and Fe_2O_3/TiO_2−P are Fe_2O_3. So, more attention was paid to the surface Fe species. However, the XPS results (Figure S6) show that the surface Fe species in FeTi-T and Fe_2O_3/TiO_2−P possess almost the same binding energy, suggesting nearly the same oxidation state of these Fe species. On the basis of this result, it is also deduced that the interaction between Fe_2O_3 and TiO_2 nanotubes should be similar to that between Fe_2O_3 and TiO_2−P. It has been reported that the large diameter of the TiO_2 nanotubes (~150 nm) can minimally induce the uneven distribution of electronic states of TiO_2 inside/outside the nanotubes, which is different from that of the carbon nanotubes with much smaller diameter (<10 nm).[36] By comparing the particle size of Fe_2O_3, it is found that the Fe_2O_3 in Fe_2O_3/TiO_2−P is even smaller than that in FeTi-T; meanwhile, the sample Fe_2O_3/TiO_2−P possesses more adsorbed oxygen species than the FeTi-T catalyst (Table 2). Nevertheless, the apparent activation energy for soot combustion over FeTi-T samples is much lower than that over Fe_2O_3/TiO_2−P (Figure S7 and Table 2), suggesting different mechanisms for soot combustion in these two catalytic systems. The structure of TiO_2 nanotubes may have played a key role during soot combustion. To clarify the function of TiO_2 nanotubes, we proposed a domain-confined multiple collision mechanism as described below. It is thought that the soot particulates falling into the nanotubes should be confined

dx.doi.org/10.1021/cs401017r | ACS Catal. 2014, 4, 934−941

in a limited space; the gas flow makes them retain Brownian-like movement in the confined space. As a result, the multiple collisions between soot particulates and anchored Fe_2O_3 nanoparticles are potential. It is well-known that the oxidation of solid particles proceeds from surface to bulk, which can hardly be finished at the moment of a single collision and which is totally different from the situation for a molecule−surface collision reaction. Therefore, it is deduced that the soot oxidation over TiO_2 nanotube-based catalysts FeTi-T may take place via the multiple collision reaction pathway. For powder catalyst Fe_2O_3/TiO_2−P, their micro- or mesopores are inaccessible to large soot particulates, decreasing the contact points; in addition, although the multiple collisions between soot particulates and catalytic sites on the outer surface of Fe_2O_3/TiO_2−P are also potential, such an opportunity should be much lower, because the soot particulates have much larger space to move in the open structure of this catalyst. On the basis of the above analysis, a domain-confined multiple-collision mechanism was proposed and visually illustrated in Scheme 1c and the Movie S1 (see SI). In summary, the better catalytic activity of Fe_2O_3/TiO_2−NA for soot combustion may arise from the confinement effect of macroporous TiO_2 nanotube structure, which can increase the contact chance and contact efficiency between soot particulates and catalytic sites. The lower apparent activation energy for the soot oxidation reaction over this catalyst is highly related to the multiple collision based reaction mechanism.

CONCLUSION

The ordered TiO_2 nanotube-array-supported Fe_2O_3 nanoparticles were successfully synthesized through a light-assisted cyclic magnetic adsorption (LCMA) method, and they were employed in catalytic soot combustion for the first time. The content and size of Fe_2O_3 nanoparticles anchored into TiO_2 nanotubes can be easily adjusted through controlling the cycles of magnetic adsorption and precursor particles. The optimal loading of Fe_2O_3 nanoparticles in Fe_2O_3/TiO_2−NA is 8 wt %. Compared with the conventional powder TiO_2 (P25) supported Fe_2O_3 catalyst, the as-prepared catalyst exhibited much better activity for soot combustion. The nanotube confinement effect on soot combustion accounts well for the enhanced activity of TiO_2 nanotube-based catalyst. A novel domain-confined multiple collision based reaction mechanism was proposed to interpret the essence of such a confinement effect. The catalyst design and preparation strategy as well as the revealed confinement effect in this work is worthy to be referenced during the exploration of other advanced catalysts used for soot combustion.

ASSOCIATED CONTENT

Supporting Information

Photo, TEM images, EDX, XPS, E_a, and Movie S1. This material is available free of charge via the Internet at http://pubs.acs.org/.

AUTHOR INFORMATION

Corresponding Author

*E-mail: mengm@tju.edu.cn.

Notes

The authors declare no competing financial interest.

ACKNOWLEDGMENTS

This work was financially supported by the National Natural Science Foundation of China (Nos. 21276184, U1332102, 21076146), the Specialized Research Fund for the Doctoral Program of Higher Education of China (No. 20120032110014), the Program of New Century Excellent Talents in the University of China (No. NCET-07-0599). The authors are also grateful to the Program of Introducing Talents of Discipline to the University of China (No. B06006).

REFERENCES

(1) Kimura, R.; Wakabayashi, J.; Elangovan, S. P.; Ogura, M.; Okubo, T. *J. Am. Chem. Soc.* **2008**, *130*, 12844−12845.
(2) Hernández-Giménez, A. M.; Castelló, D. L.; Bueno-López, A. *Chem. Papers* **2013**, DOI: 10.2478/s11696-013-0469-7.
(3) Bueno-López, A. *Appl. Catal., B* **2014**, *146*, 1−11.
(4) Russell, A.; Epling, W. S. *Catal. Rev.: Sci. Eng.* **2011**, *53*, 337−423.
(5) Stanmore, B. R.; Brilhac, G. F.; Gilot, P. *Carbon* **2001**, *39*, 2247−2268.
(6) Wu, X. D.; Lin, F.; Weng, D.; Li, J. *Catal. Commun.* **2008**, *9*, 2428−2432.
(7) Harrison, P. G.; Ball, I. K.; Daniell, W.; Lukinskas, P.; Céspedes, M.; Miró, E. E.; Ulla, M. A. *Chem. Eng. J.* **2003**, *95*, 47−55.
(8) Zhang, G.; Zhao, Z.; Liu, J.; Jiang, G.; Duan, A.; Zheng, J. X.; Chen, S. L.; Zhou, R. X. *Chem. Commun.* **2010**, *46*, 457−459.
(9) Li, Z. Q.; Meng, M.; Zha, Y. Q.; Dai, F. F.; Hu, T. D.; Xie, Y. N.; Zhang, J. *Appl. Catal., B* **2012**, *121*, 65−74.
(10) Wang, Q.; Chung, J. S.; Guo, Z. H. *Ind. Eng. Chem. Res.* **2011**, *50*, 8384−8388.
(11) Samir, B.; Nunzio, R.; Debora, F. *Catal. Today* **2013**, *216*, 57−63.
(12) Aneggi, E.; Wiater, D.; Leitenburg, C.; Llorca, J.; Trovarelli, A. *ACS Catal.* **2014**, *4*, 172−181.
(13) Mul, G.; Kapteijn, F.; Moulijn, J. A. *Appl. Catal., B* **1997**, *12*, 33−47.
(14) Querini, C. A.; Ulla, M. A.; Requejo, F.; Soria, J.; Sedran, U. A.; Miro, E. E. *Appl. Catal., B* **1998**, *15*, 5−19.
(15) Badini, C.; Saracco, G.; Serra, V.; Specchia, V. *Appl. Catal., B* **1998**, *18*, 137−150.
(16) van Setten, B.; van Dijk, R.; Jelles, S. J.; Makkee, M.; Moulijn, J. A. *Appl. Catal., B* **1999**, *21*, 51−61.
(17) Wang, Q.; Xing, Z. P.; Zhang, W. W.; Guo, Z. H.; Chung, J. S. *Sci. Adv. Mater.* **2011**, *3*, 989−993.
(18) Mul, G.; Neeft, J. P. A.; Kapteijn, F.; Makkee, M.; Moulijn, J. A. *Appl. Catal., B* **1995**, *6*, 339−352.
(19) Badini, C.; Serra, V.; Saracco, G.; Montorsi, M. *Catal. Lett.* **1996**, *37*, 247−254.
(20) Wei, Y. C.; Liu, J.; Zhao, Z.; Chen, Y. S.; Xu, C. M.; Duan, A. J.; Jiang, G. Y.; He, H. *Angew. Chem., Int. Ed.* **2011**, *50*, 2326−2329.
(21) Xu, J. F.; Liu, J.; Zhao, Z.; Xu, C. M.; Zheng, J. X.; Duan, A. J.; Jiang, G. Y. *J. Catal.* **2011**, *282*, 1−12.
(22) Legutko, P.; Stelmachowski, P.; Trebala, M.; Sojka, Z.; Kotarba, A. *Top. Catal.* **2013**, *56*, 489−492.
(23) Yu, Y. F.; Ren, J. L.; Meng, M. *Int. J. Hydrogen Energy* **2013**, *38*, 12266−12272.
(24) Polshettiwar, V.; Varma, R. S. *Org. Biomol. Chem.* **2009**, *7*, 37−40.
(25) Ozawa, T. *J. Therm. Anal. Calorim.* **1970**, *2*, 301−324.
(26) Ozawa, T. *J. Therm. Anal. Calorim.* **1975**, *7*, 601−617.
(27) Ahniyaz, A.; Sakamoto, Y.; Bergstrom, L. *Cryst. Growth Des.* **2008**, *8*, 1798−1800.
(28) He, Q. L.; Yuan, T. T.; Wei, S. Y.; Haldolaarachchige, N.; Luo, Z. P.; Young, D. P.; Khasanov, A.; Guo, Z. H. *Angew. Chem.* **2012**, *124*, 8972−8975.
(29) Guan, K. *Surf. Coat. Technol.* **2005**, *191*, 155−160.
(30) Nakajima, A.; Hashimoto, K.; Watanabe, T. *Langmuir* **2000**, *16*, 7044−7047.

(31) Bourgeois, F.; Gergaud, P.; Renevier, H.; Leclere, C.; Feuillet, G. *J. Appl. Phys.* **2013**, *113*, 013510.
(32) Okudera, H.; Yoshiasa, A.; Murai, K.; Okube, M.; Takeda, T.; Kikkawa, S. *J. Mineral. Petrol. Sci.* **2012**, *107*, 127−132.
(33) Wang, Q. R.; Yang, X. C.; Liu, D.; Zhao, J. F. *J. Alloys Compd.* **2012**, *527*, 106−111.
(34) Mohapatra, S. K.; Kondamudi, N.; Banerjee, S.; Misra, M. *Langmuir* **2008**, *24*, 11276−11281.
(35) Yu, J. G.; Dai, G. P.; Huang, B. B. *J. Phys. Chem. C* **2009**, *113*, 16394−16401.
(36) Pan, X. L.; Fan, Z. L.; Chen, W.; Ding, Y. J.; Luo, H. Y.; Bao, X. H. *Nat. Mater.* **2007**, *6*, 507−511.
(37) Baker, R. T. K.; Harris, P. S. *J. Phys. E: Sci. Instrum.* **1972**, *5*, 793−797.
(38) Goethel, P. J.; Yang, R. T. *J. Catal.* **1989**, *119*, 201−214.
(39) Cooper, B. J.; Thoss, J. E. *SAE Int.* **1989**, DOI: 10.4271/890404.
(40) Baumgarten, E.; Schuck, A. *Appl. Catal.* **1988**, *37*, 247−257.
(41) Baker, R. T. K.; Chludzinski, J. J. *Carbon* **1981**, *19*, 75−82.
(42) Mul, G.; Kapteijn, F.; Doornkamp, C.; Moulijn, J. A. *J. Catal.* **1998**, *179*, 258−266.